Journal of Science and Transport Technology
Journal homepage: https://jstt.vn/index.php/en

UNIVERSITY OF TRANSPORT TECHNOLOGY

Enhancing Seismic Performance of Reinforced Concrete Exterior Joints with Ultra-high-performance Steel Fiber Reinforced Concrete: A Parametric Finite Element Study

Trung-Hieu Tran
Faculty of Civil Engineering, Hanoi Architectural University, Km10 NguyenTrai Road, Hanoi 100000, Viet Nam

Article info
Type of article:
Original research paper

DOI:
https://doi.org/10.58845/jstt.utt.2025.en.5.2.31-47

***Corresponding author:**
Email address:
hieutt@hau.edu.vn

Received: 13/03/2025
Received in Revised Form: 17/04/2025
Accepted: 24/04/2025

Abstract: Beam-column joints are vital to the stability and performance of reinforced concrete (RC) frame structures, particularly under seismic conditions. Understanding their stress-strain behavior is crucial for evaluating their capacity and ductility. However, performing detailed experimental studies with numerous specimens is often impractical due to significant costs and time constraints. As a result, finite element (FE) analysis, supported by tools like ABAQUS, has become a preferred approach for studying joint behavior effectively. This study employs the finite element method (FEM) to analyze exterior beam-column joints designed for high ductility (DCH) and enhanced with ultra-high-performance steel fiber reinforced concrete (UHPSFRC). The FE results are validated against experimental data through comparisons of load-displacement responses, failure patterns, and reinforcement strain progression. Furthermore, the research examines the effects of parameters like UHPSFRC strengthening length, axial column load, and steel fiber content on joint tensile stress, providing insights into optimizing seismic performance.

Keywords: Ultra-high-performance concrete; Exterior beam-column joint; Reversed cyclic loading; Crack patterns; Reinforcement strain development; Finite element analysis.

1. Introduction

Beam-column joints in reinforced concrete (RC) frame structures serve as critical nodes that ensure structural integrity and facilitate load transfer between horizontal and vertical elements, particularly under seismic loading conditions. These joints, categorized geometrically into corner, exterior, and interior types, are subjected to complex stress states during earthquakes, making their behavior a focal point of structural engineering research [1]. The performance of these joints can dictate the overall stability of a frame, as failure at the joint region often precipitates progressive collapse under dynamic loads [2]. Historically, joints exhibit elastic behavior when beams, columns, and the joint core remain undamaged and free of plastic deformations. However, the onset of cracking in concrete or yielding of reinforcement marks a transition to plastic behavior, necessitating a deeper understanding of their mechanical response [3].

The study of beam-column joint behavior

dates back to seminal works in the late 20th century. Paulay et al. pioneered the analysis of force components in exterior joints, proposing a model that accounted for shear and axial forces within the joint region [4]. This foundational work was later expanded by Hakuto et al., who introduced a refined approach to calculate principal compressive (p_c) and tensile (p_t) stresses at mid-joint height, incorporating the influence of axial column stress (f_a) [5]. These stresses, alongside joint geometry (e.g., width w_j), define the nominal shear stress (v_{jh}), a key indicator of shear resistance [5]. This evolution in understanding has spurred the development of various shear resistance models over the decades, reflecting the growing complexity of seismic design requirements.

Recent studies have produced a spectrum of shear models, including empirical formulations [6], strut-and-tie models [7], and average plane stress approaches [8]. Empirical models often rely on experimental data to correlate shear strength with material properties, such as the square root of concrete compressive strength [9]. Strut-and-tie models, on the other hand, idealize force paths within the joint, offering a mechanistic perspective that has gained traction in recent studies [10]. Plane stress models provide a broader stress distribution analysis, proving useful for complex geometries [11]. Despite these advances, a significant limitation persists: few models comprehensively address both ultimate strength and serviceability limit states, such as the onset of diagonal cracking, which reduces joint stiffness and initiates plastic behavior [12]. This cracking threshold, often observed as the first diagonal crack, is critical as it signals a shift in load-carrying mechanisms [13].

Design codes like ACI 318-14 [14] and NZS 3101 [15] have incorporated some of these findings, emphasizing tensile strength (f_{ct}) and geometric ratios (h_b/h_c) alongside compressive strength. However, gaps remain in accounting for critical parameters such as axial load effects (f_a), anchorage details, and principal tensile stress (p_t), which are pivotal in predicting joint failure [16]. The principal tensile stress (p_t), in particular, integrates the influence of axial load and serves as a reliable indicator of impending joint distress, a concept increasingly adopted in modern standards. Recent research has highlighted the need to address these deficiencies, especially in the context of seismic retrofitting, where traditional RC joints often exhibit inadequate ductility and shear capacity [17].

The introduction of advanced materials, such as ultra-high-performance steel fiber reinforced concrete (UHPSFRC), has opened new avenues for enhancing joint performance. UHPSFRC, characterized by its exceptional compressive strength, tensile capacity, and ductility due to steel fiber reinforcement, has been shown to significantly improve the seismic resilience of RC structures [18]. Experimental studies have demonstrated its ability to mitigate cracking and enhance energy dissipation in beam-column joints under cyclic loading [19]. However, conducting large-scale experimental programs to explore UHPSFRC's full potential is often impractical due to high costs, lengthy construction times, and resource constraints. Consequently, finite element (FE) analysis has emerged as a powerful tool to complement experimental efforts, offering a cost-effective means to simulate joint behavior and evaluate parametric influences [20].

Recent numerical studies have leveraged FE methods to investigate UHPSFRC-strengthened joints, validating simulations against experimental benchmarks [12,21]. These studies underscore the importance of accurately modeling material nonlinearity, crack propagation, and reinforcement interaction, challenges that modern software like ABAQUS adeptly addresses [21].

Despite these advancements, there is a lack of systematic studies that comprehensively analyze the combined effects of UHPSFRC strengthening length, axial column load, and steel fiber content on the seismic performance of exterior beam-column joints designed for high ductility (DCH). Experimental investigations are often constrained by high costs and time, limiting the scope of parametric studies. Moreover, existing numerical models rarely integrate all these parameters to predict principal tensile stress and failure patterns under reversed cyclic loading, a critical aspect of seismic design.

This study addresses these gaps by employing finite element (FE) analysis in ABAQUS to simulate UHPSFRC-strengthened exterior beam-column joints under cyclic loading. Unlike previous research, it systematically investigates the interplay of UHPSFRC strengthening length, axial load, and steel fiber content, validated against experimental data. The novelty lies in the development of a robust FE model that accurately captures load-displacement responses, crack patterns, and reinforcement strains, offering a cost-effective alternative to extensive experimental testing. The study's contributions include: (1) a validated FE framework for seismic analysis of UHPSFRC-strengthened joints, (2) parametric insights into optimizing joint design for enhanced ductility and shear resistance, and (3) practical guidance for retrofitting RC structures in earthquake-prone regions, advancing seismic engineering practices.

The study validates FE results against experimental data, focusing on load-displacement relationships, failure patterns, and reinforcement strain development. CDP parameters were calibrated from experimental stress-strain curves, ensuring accuracy in simulating nonlinear behavior, with key values (ψ = 36°, e = 0.1, fb0/fc0 = 1.16). These curves were adjusted for fracture energy and mesh size dependency to ensure accurate numerical simulation. Furthermore, it conducts a parametric analysis to assess the effects of UHPSFRC strengthening length, axial column load, and steel fiber content on principal tensile stress (pt) within the joint region. By addressing these factors, this work aims to contribute to the growing body of knowledge on seismic retrofitting, offering practical insights for engineers seeking to enhance the resilience of RC frames in earthquake-prone regions [5].

2. Materials and Methods

This study developed a finite element (FE) model in ABAQUS to simulate the seismic behavior of exterior beam-column joints designed for high ductility (DCH) and strengthened with ultra-high-performance steel fiber reinforced concrete (UHPSFRC). The following subsections detail the problem setup and the mathematical principles underlying the FEM model.

2.1. Problem Setup

The numerical model replicates an exterior beam-column joint, comprising a column (300 mm x 300 mm cross-section, 1800 mm height) and a beam (250 mm x 400 mm cross-section, 1500 mm length) forming a T-shaped joint, reflecting typical RC frame structures (Fig. 1). Conventional concrete has a compressive strength of 30 MPa (Figs. 2a–b), while UHPSFRC ranges from 135.93 to 151.62 MPa (Table 4), with enhanced tensile strength. Steel reinforcement follows a bilinear elastic-plastic model (Fig. 3) with an elastic modulus of 200 GPa and yield strength of 400 MPa.

Loading includes an axial load at the column top (0 to 0.15 Agfc') and cyclic lateral displacement at the beam end (up to 6.5% drift) to simulate seismic conditions. Boundary conditions use reference points: RP1 for axial load, RP2 for cyclic displacement, and RP3 at the column base restricting translation but allowing rotation (Fig. 1c).

The model uses C3D8R elements for concrete and UHPSFRC, and T3D2 elements for reinforcement, with embedded interaction. Mesh sizes are 50 mm outside the joint and 25 mm within it (Fig. 1b) for accuracy. Steel plates at load points use rigid tie constraints.

2.2. Mathematical Principles of the FEM Model

The FEM model in ABAQUS solves the equilibrium of forces using the principle of virtual work, discretizing the joint into finite elements with shape functions to approximate displacements and strains. The ABAQUS/Explicit solver handles material nonlinearity, updating stiffness iteratively based on constitutive models.

Concrete and UHPSFRC are modeled using the Concrete Damage Plasticity (CDP) model, capturing compressive crushing and tensile cracking with stress-strain curves (Figs. 2a–b for concrete, Figs. 4a–b for UHPSFRC). The CDP model uses isotropic damaged elasticity and plasticity, with parameters (ψ = 36°, e = 0.1, fb0/fc0 = 1.16) calibrated from experimental data. UHPSFRC's tensile behavior accounts for fracture energy to model crack propagation, adjusted for mesh size dependency.

Steel reinforcement is modeled as bilinear elastic-plastic, with stresses computed based on truss element deformations. The explicit solver ensures stability for cyclic loading, with slow rates to mimic quasi-static conditions.

The nonlinear stress-strain behavior of concrete (Figs. 2a–b for conventional concrete; Figs. 3a–b for UHPSFRC) was modeled using the CDP model, capturing elastic, plastic, and softening phases with experimental stress-strain data and damage parameters (ψ = 36°, e = 0.1, fb0/fc0 = 1.16). For conventional concrete, CDP reflected brittle tensile failure and compressive crushing; for UHPSFRC, it accounted for enhanced tensile strength and ductility. The study focused on material nonlinearity, as drift ratios (up to 6.5%) minimized geometric nonlinearity effects. Small deformation theory was used in ABAQUS/Explicit for stability.

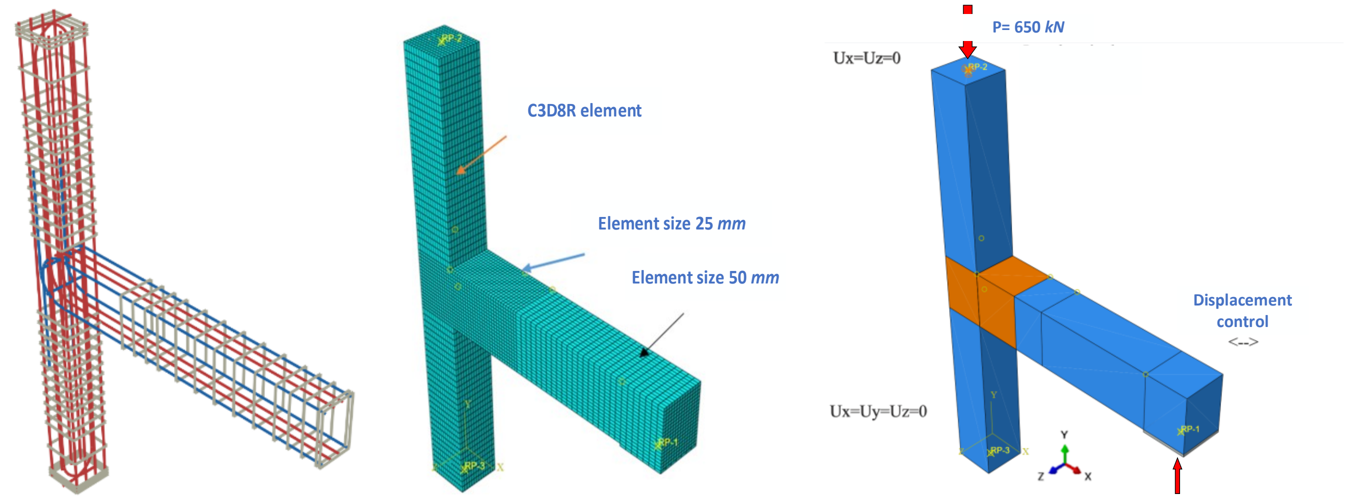

a) Reinforcement element (T3D2)
b) Concrete elements (C3D8R) and geometric meshing
c) Boundary conditions imposed on the finite element model

Fig. 1. Force components acting on exterior frame nodes

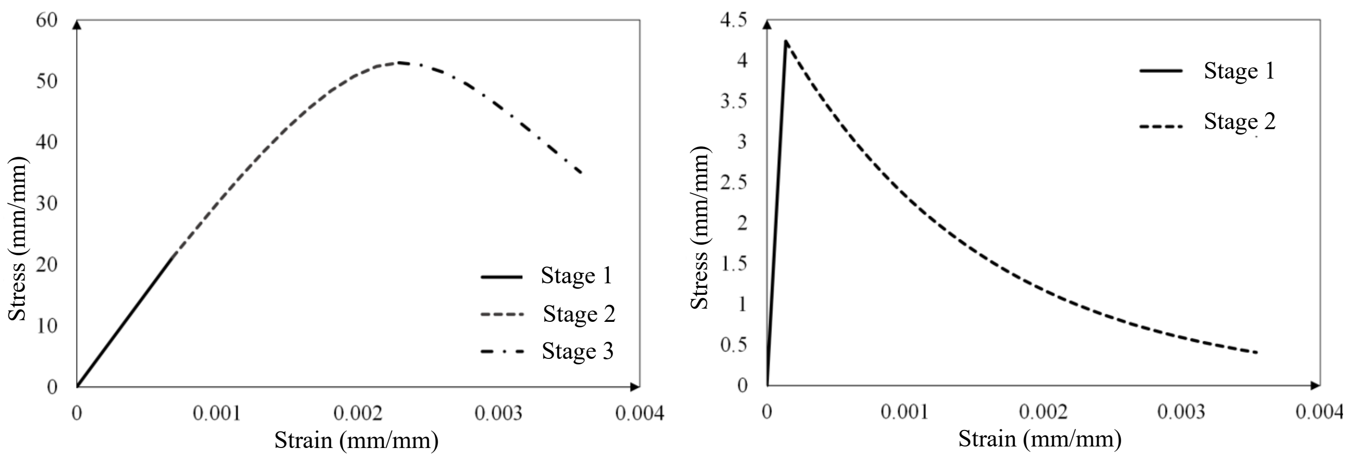

a) Compression behavior
b) Tension behavior

Fig. 2. Stress-strain relationship of concrete

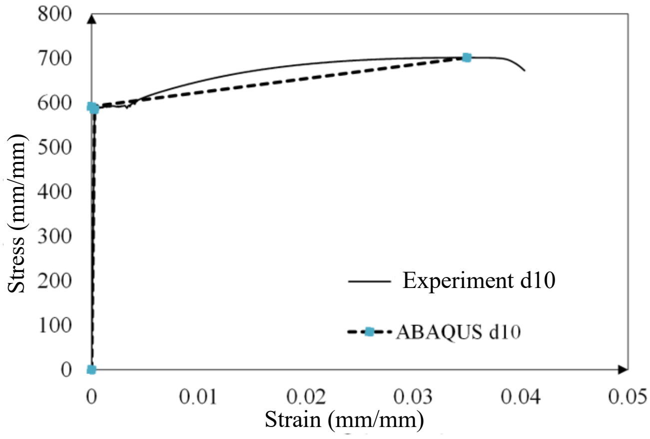

Fig. 3. Stress-strain relationship of steel

Boundary conditions (Fig. 1c) utilized reference points: RP1 applied an axial load at the column top, RP2 imposed cyclic lateral displacement at the beam end, and RP3 at the column base restricted translation while allowing rotation. Bi-directional cyclic displacement was applied at RP2 to replicate quasi-static reversed loading. The ABAQUS/Explicit solver with slow loading rates ensured convergence, with drift ratio (Δl/lb) presented in Eq. (1) quantifying deformation.

$$\text{Drift ratio} = \frac{\Delta_l}{0.5 l_b} \times 100\% \quad (1)$$

where: Δ_l is the beam end displacement and l_b is the beam length.

3. Results and discussion

Boundary conditions, shown in Fig. 1c, utilized reference points: RP1 applied an axial load at the column top, RP2 imposed cyclic lateral displacement at the beam end, and RP3 at the column base restricted translation while allowing rotation. Bi-directional cyclic displacement was applied at RP2 to replicate quasi-static reversed loading in both directions. The ABAQUS/Explicit solver with slow loading rates ensured convergence, with drift ratio (Δ_l/l_b) presented in Eq. (1) quantifying deformation. Slow rates minimized inertial effects, ensuring quasi-static conditions. This setup supports accurate simulation of joint behavior.

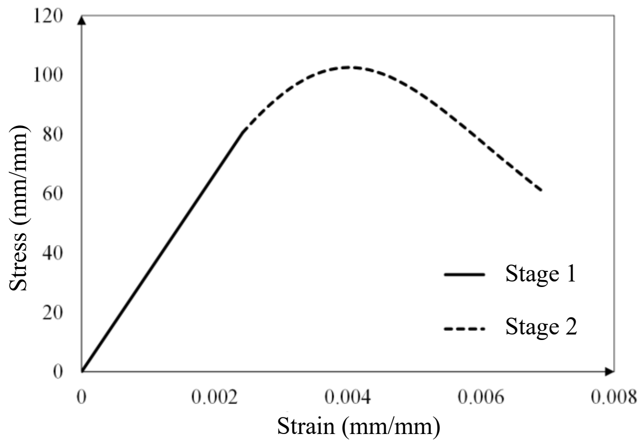

a) Compression behavior

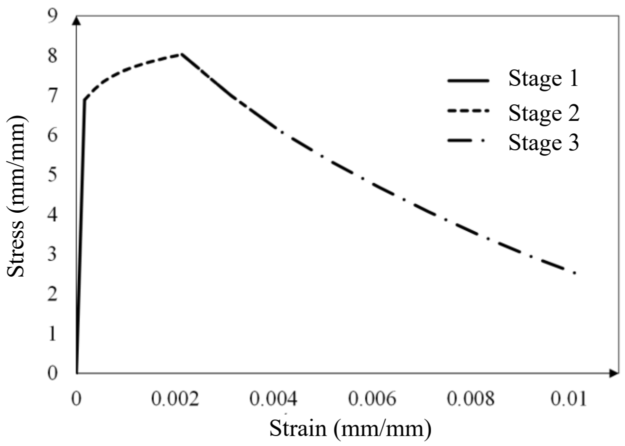

b) Tension behavior

Fig. 4. Stress-strain relationship of concrete

3.1. FE Simulation and validation

The FE model was validated against experimental data to ensure its accuracy in predicting the behavior of UHPSFRC-strengthened exterior beam-column joints under cyclic loading. Validation involved comparing FE outputs with experimental results for three specimens: a control specimen (S1) with conventional concrete, a strengthened specimen (S2) with UHPSFRC applied over a fixed length, and a variably strengthened specimen (S3) with different UHPSFRC lengths. The comparisons focused on three key metrics: load-displacement responses, reinforcement strains, and crack patterns, as illustrated in Figs. 5-10. The validation process assessed the model's ability to capture nonlinear behavior, including stiffness, peak load, ductility, and failure modes, with quantitative metrics to evaluate agreement.

Validating the FE model against experimental data ensures its accuracy in predicting UHPSFRC-strengthened exterior beam-column joint behavior under cyclic loading. This section examines results for three specimens—control (S1), strengthened (S2), and variably strengthened (S3)—comparing FE outputs with experimental results for load capacity, reinforcement strains, and crack patterns, as shown in Figs. 5-10. The process confirms the model's reliability for further analysis.

For the control specimen (S1), mesh sizes of 25 mm, 50 mm, and 100 mm were tested, with the 25 mm mesh providing the closest match to experimental load-displacement curves, as shown in Fig. 5a and Table 1. The 25 mm mesh was selected as it aligns with the concrete's characteristic length, minimizing localization effects in the Concrete Damage Plasticity (CDP) model. The FE model predicted peak loads within 6% of experimental values (e.g., 72 kN vs. 76 kN at 2.2% drift), with a correlation coefficient of 0.98 for the load-displacement curve up to 2.2% drift. This size aligns with the concrete's characteristic length, minimizing localization effects in the CDP model. Peak load differences were below 6% up to 2.2% drift, though initial stiffness was overestimated due to idealized material assumptions, a finding consistent with [11]. Reinforcement strains, plotted in Fig. 7b, aligned with experimental data within 6% until 2.2% drift, after which yielding caused rapid increases. Crack patterns, illustrated in Fig. 8, evolved from initial cracks at P ≤ 70 kN (a) to shear cracks at 1.4% drift (b), widespread joint damage at 2.2% drift (c), and ultimate shear failure at 5% drift (d), matching experimental observations. The FE model accurately captured the shear-dominated failure mode, with crack locations and propagation sequences closely resembling experimental results, though minor discrepancies in crack width were noted due to idealized fracture energy assumptions. In Fig. 6, cracks concentrate on the beam's bottom surface due to tensile stresses from cyclic loading, with maximum tension occurring near the joint under high bending moments. The longitudinal reinforcement bars are equal in the top and bottom layers to ensure symmetric resistance to positive and negative moments, facilitating consistent behavior under reversed cyclic loading. Shear reinforcement was omitted near the joint to assess UHPSFRC's role in enhancing shear capacity, reflecting deficiencies in older RC structures (Figs. 6, 8, 10).

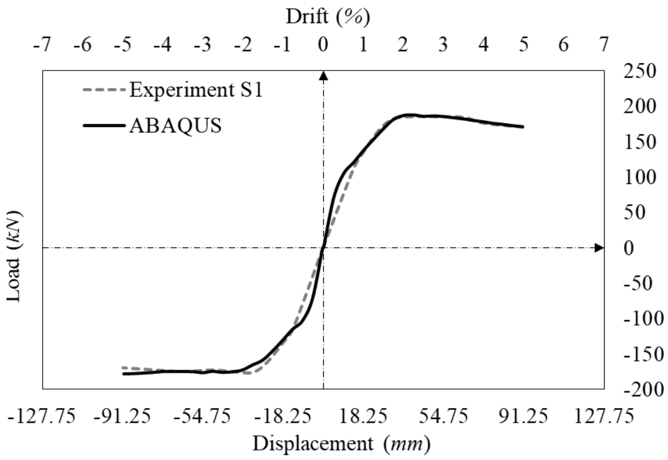

a) Force-drift relationship of the S1 model

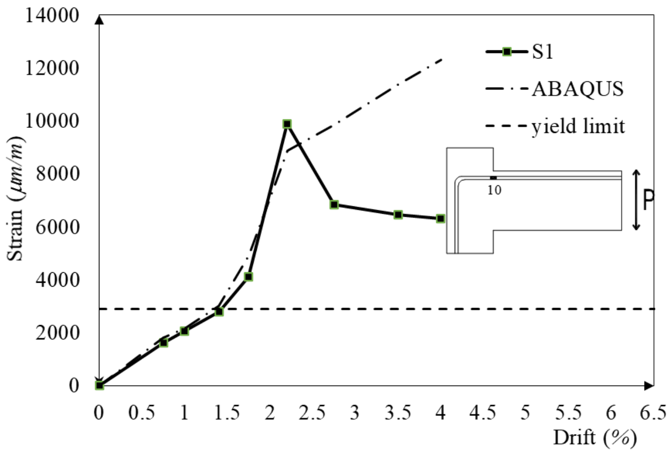

b) Development of beam reinforcement deformation of specimen S1

Fig. 5. Relationship between force – drift – deformation of steel reinforcement of specimen S1

The strengthened specimen (S2) with UHPSFRC showed similar accuracy with the 25 mm mesh, as evidenced by load-drift curves in Fig. 7a and Table 2, with differences below 5%. The FE peak load was 92 kN compared to 88 kN experimentally at 2.2% drift, with a correlation coefficient of 0.97. The model slightly overestimated initial stiffness by 8%, likely due to idealized bond assumptions between UHPSFRC and reinforcement. Reinforcement strains, shown in Fig. 7b, followed experimental trends with a maximum 15% deviation at peak load, reflecting UHPSFRC's delay in yielding. Crack evolution, depicted in Fig. 8, progressed from initial cracks at P ≤ 90 kN (a) to shear cracks at 1.4% drift (b), extensive joint damage at 2.2% drift (c), and shear failure at 6.5% drift (d).

For the variably strengthened specimen (S3), the 25 mm mesh maintained precision, with load capacities within 4% of experimental values, as shown in Fig. 9a and Table 3. Strains, plotted in Fig. 9b, deviated by up to 10% at 2.2% drift, capturing variable strengthening effects. Crack patterns, illustrated in Fig. 10, showed initial cracks at P ≤ 90 kN (a), shear cracks at 1.4% drift (b), joint-wide damage at 2.2% drift (c), and shear failure at 6.5% drift (d), consistent with experimental shear-dominated failure. These results across all specimens validate the FE model's ability to replicate complex behaviors.

Table 1. Simulation results and experimental results of sample S1

Load direction		FEM/ Test			Secant hardness		
		25 mm	50 mm	100 mm	25 mm	50 mm	100 mm
Push direction	Average	1.01	1.04	1.07	1.01	1.04	1.07
	Difference (%)	0.77	3.64	6.45	1.28	4.13	6.93
Pull direction	Average	1.02	1.10	1.12	1.02	1.12	1.13
	Difference (%)	1.51	9.45	10.95	2.01	10.79	11.40

ABAQUS Test

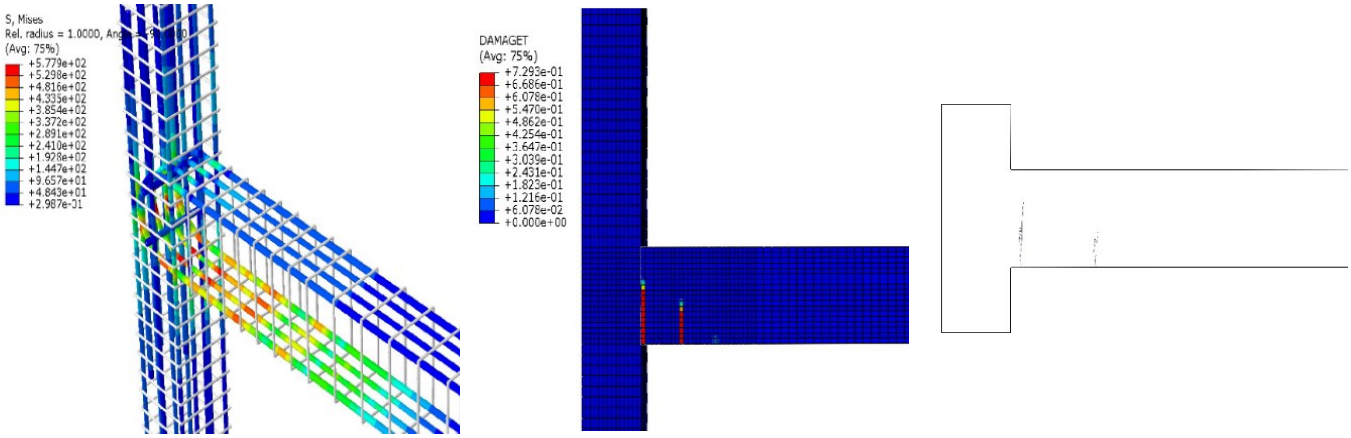

P ≤ 70 kN P ≤ 60 kN

a) First crack appeared

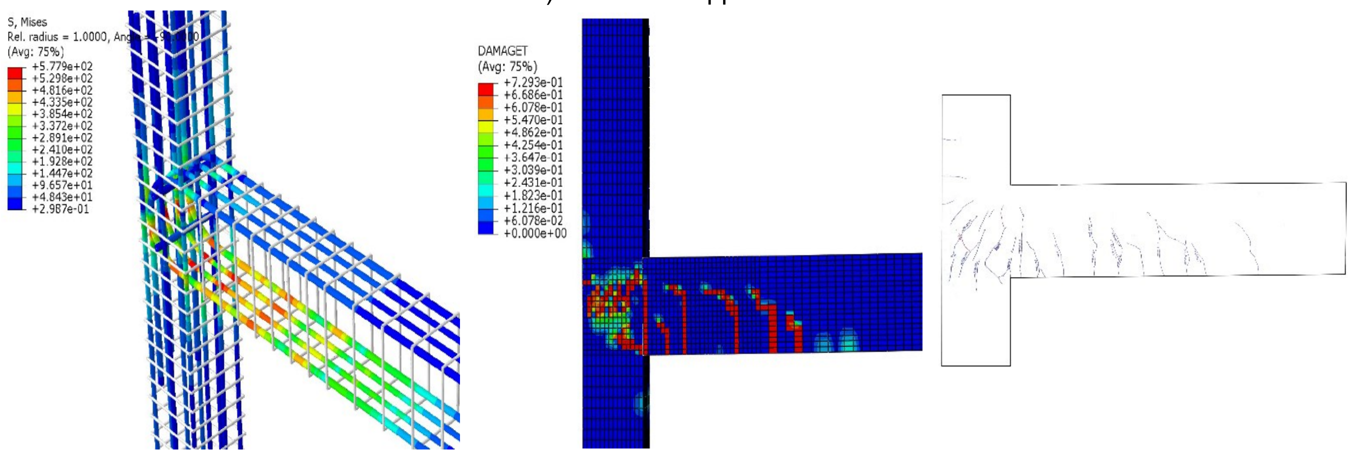

P = 168.8 kN P = 167.5 kN

b) Drift 1.4%

Fig. 6. Comparison of crack shape between experiment and FEM model of the sample S1

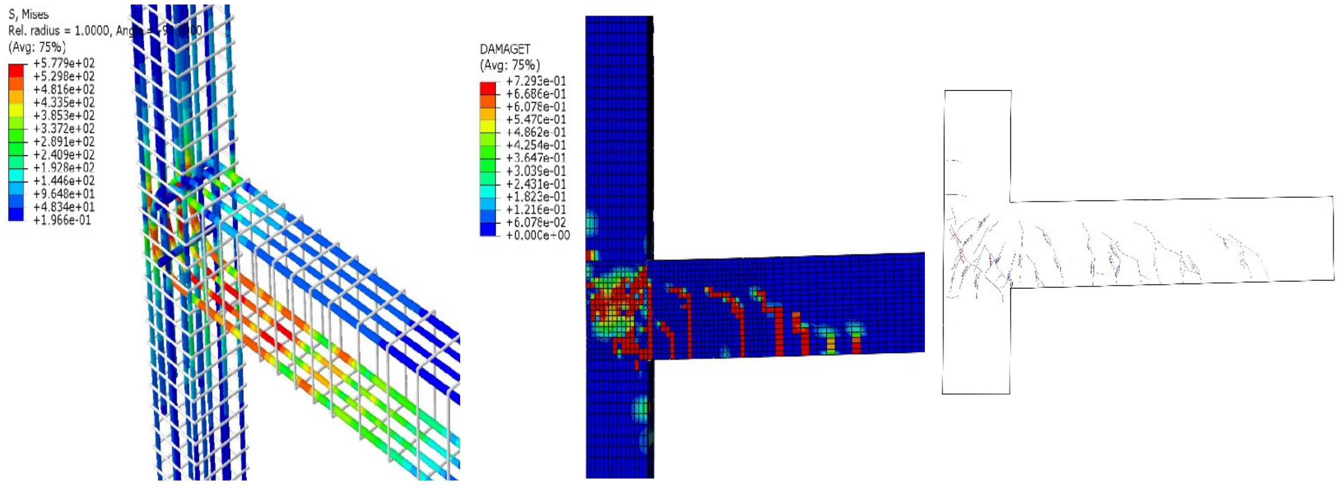

P = 187.25 kN P = 185.8 kN

c) Drift 2.2%

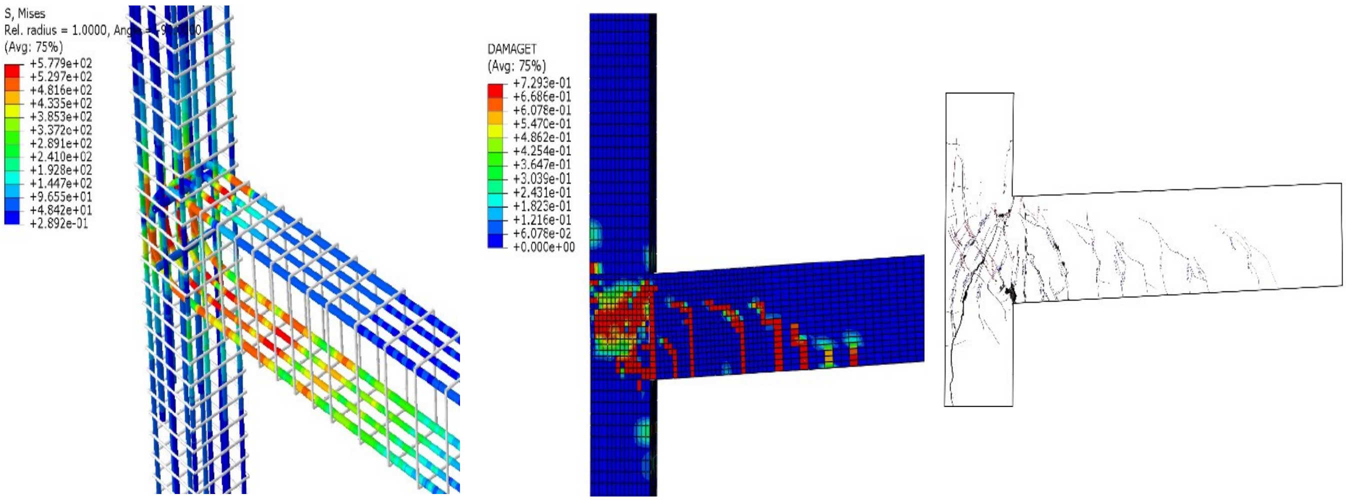

P = 170.7 kN P = 170.8 kN

d) Drift 5%

Fig. 6. (continued)

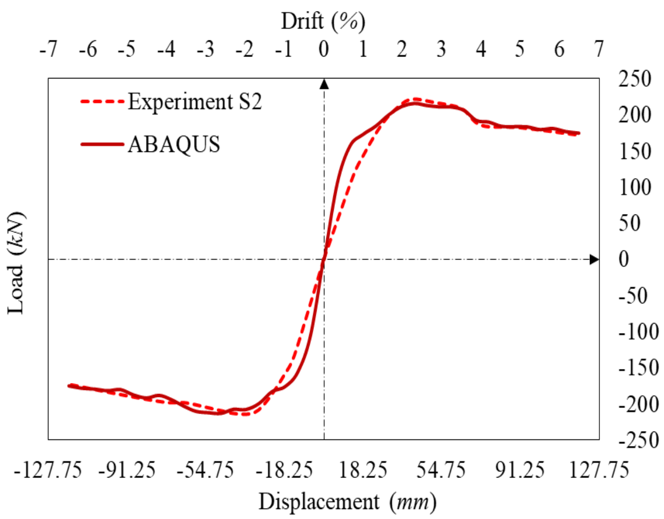

a) Force-drift relationship of the S2 model

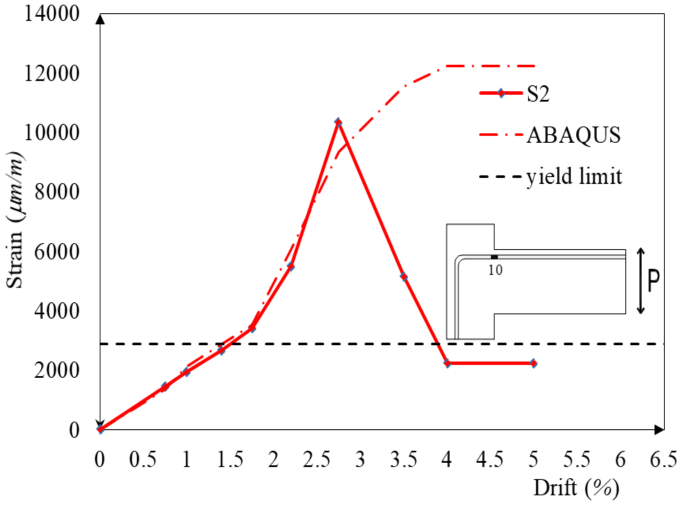

b) Development of beam reinforcement deformation of specimen S2

Fig. 7. Relationship between force – drift – deformation of steel reinforcement of specimen S2

Table 2. Simulation results and experimental results of sample S2

Load direction		FEM/ Test			Secant hardness		
		25 mm	50 mm	100 mm	25 mm	50 mm	100 mm
Push direction	Average	0.98	1.05	1.08	0.98	1.06	1.11
	Difference (%)	-2.31	5.11	7.78	-2.05	5.32	8.68
Pull direction	Average	1.00	1.08	1.14	1.00	1.08	1.15
	Difference (%)	-0.13	7.16	12.66	0.13	7.38	12.94

ABAQUS Test

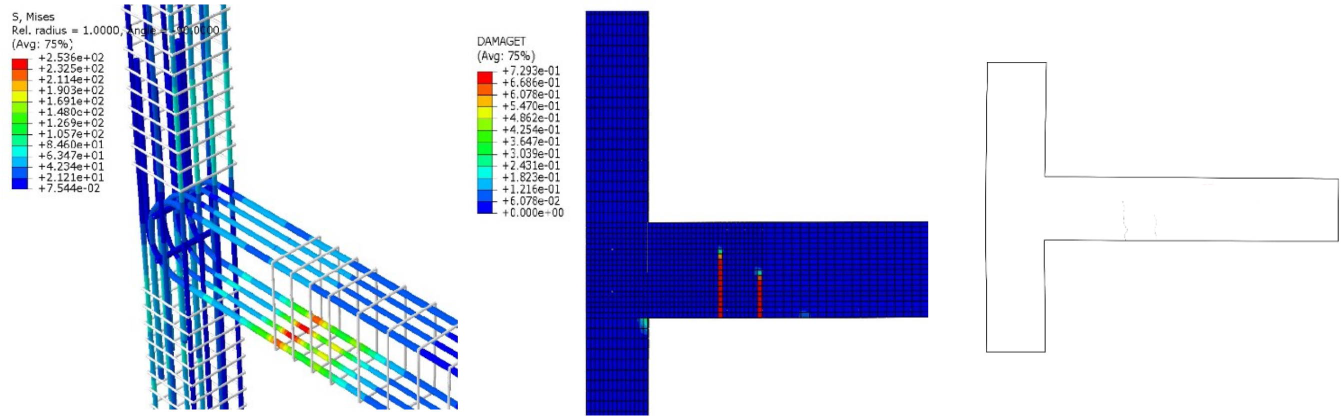

P ≤ 90 kN P ≤ 80 kN

a) First crack appeared

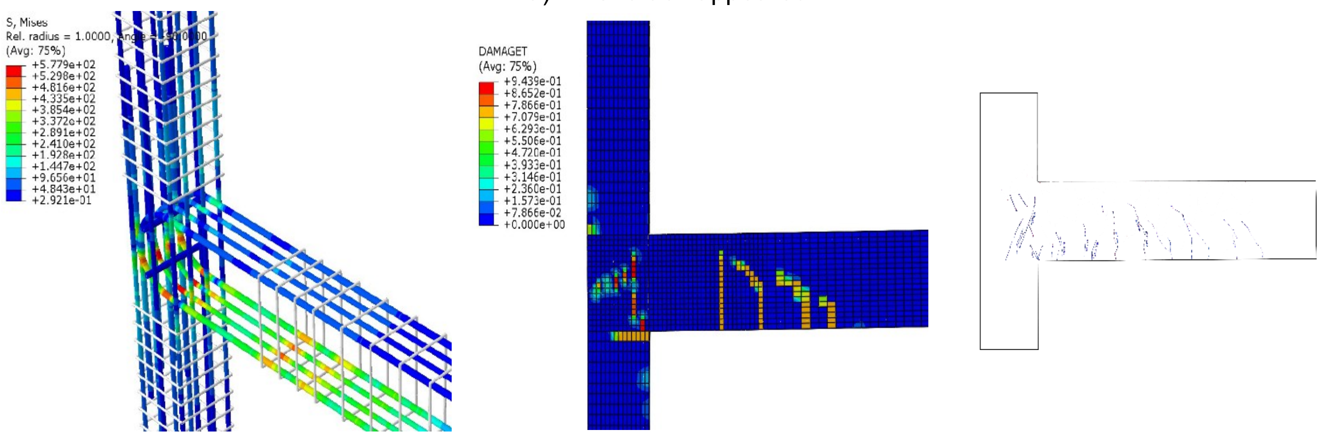

P =184.34 kN P = 180.6 kN

b) Drift 1.4%

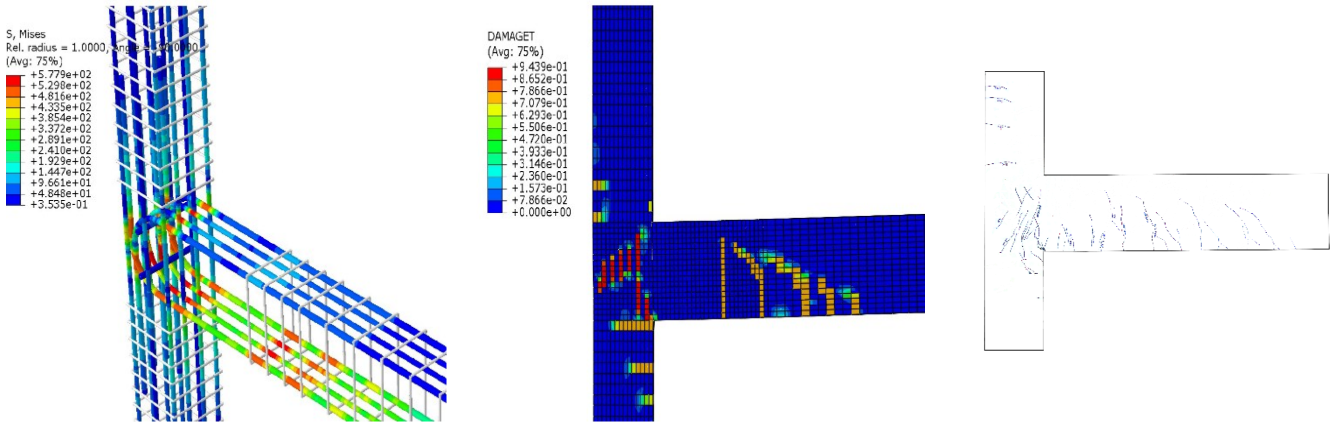

P = 215.82 kN P = 220.8 kN

c) Drift 2.2%

Fig. 8. Comparison of crack shape between experiment and FEM model of the sample S2

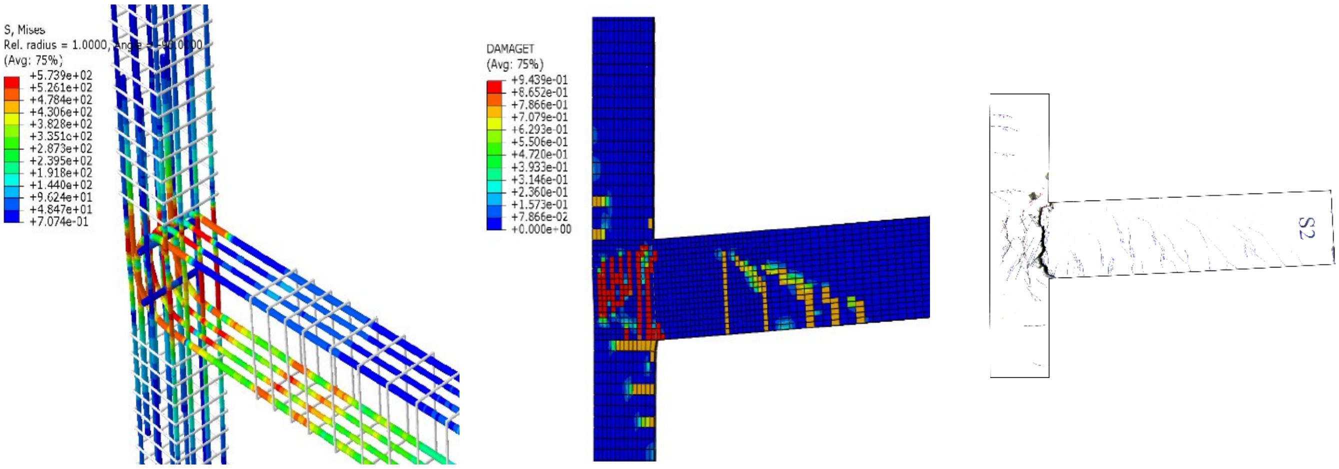

P = 174.67 kN P = 171.4 kN

d) Drift 6.5%

Fig. 8. (continued)

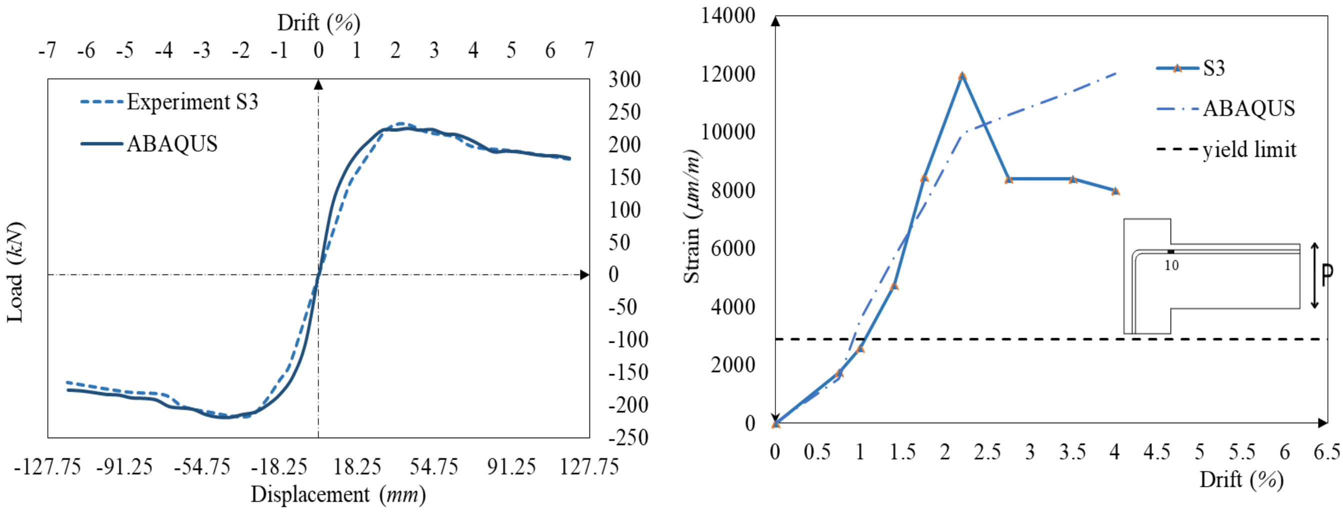

a) Force-drift relationship of the S3 model b) Development of beam reinforcement deformation of specimen S3

Fig. 9. Relationship between force – drift – deformation of steel reinforcement of specimen S3

ABAQUS Test

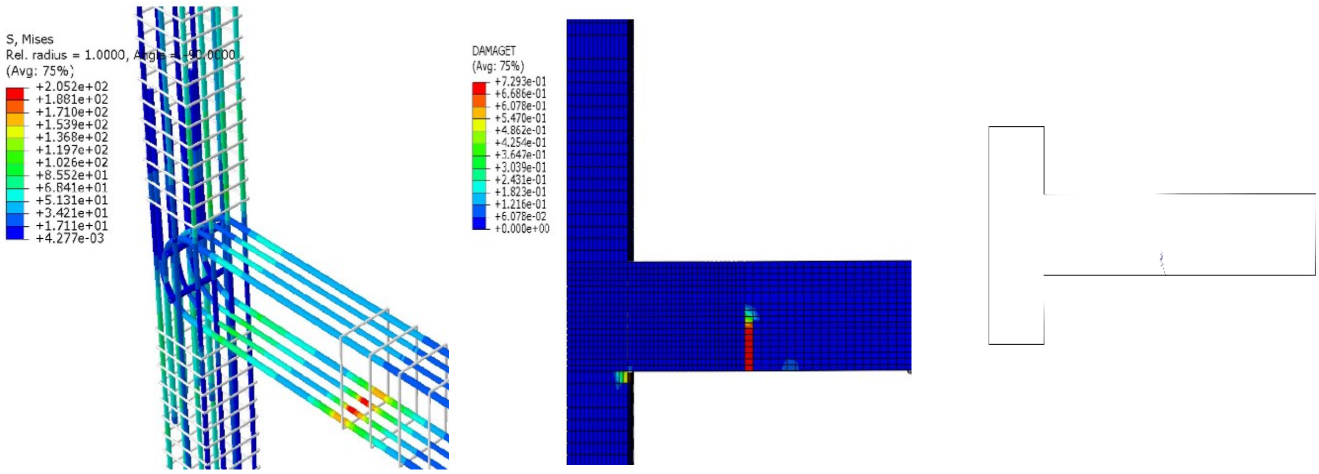

P ≤ 90 kN P ≤ 80 kN

a) First crack appeared

Fig. 10. Comparison of crack shape between experiment and FEM model of the sample S3

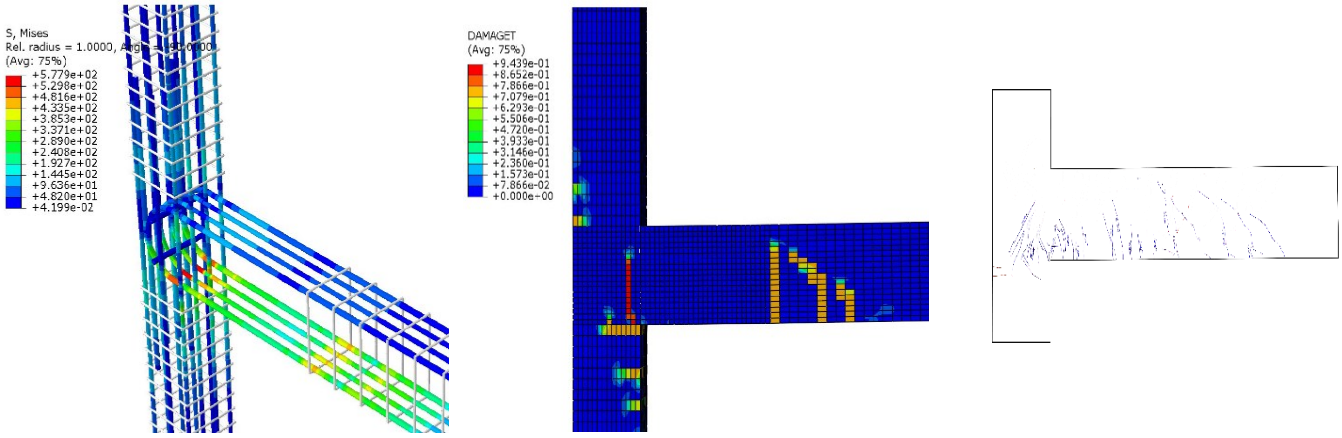

P = 206.11 kN P = 193.9 kN

b) Drift 1.4%

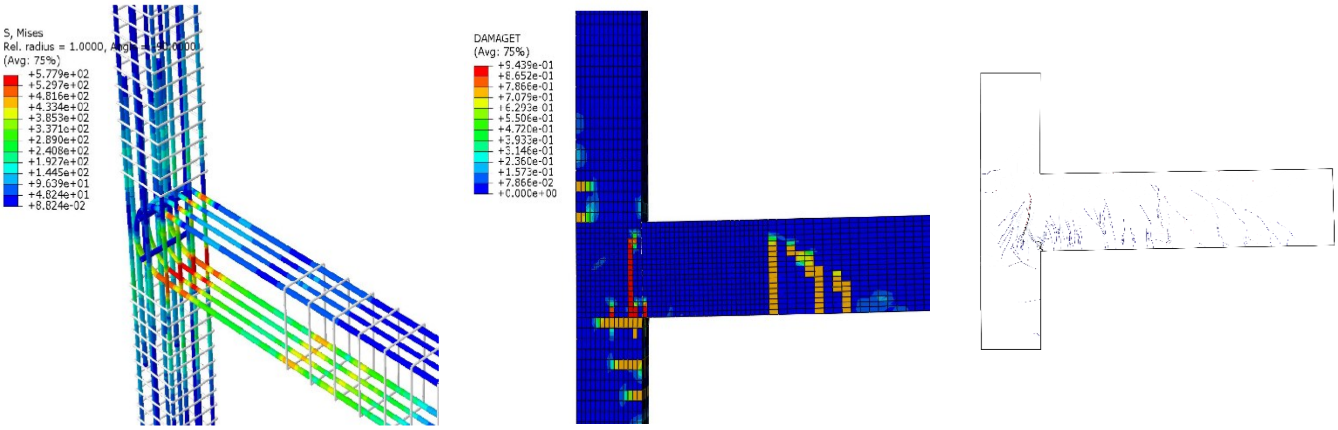

P = 224.66 kN P = 231.4 kN

c) Drift 2.2%

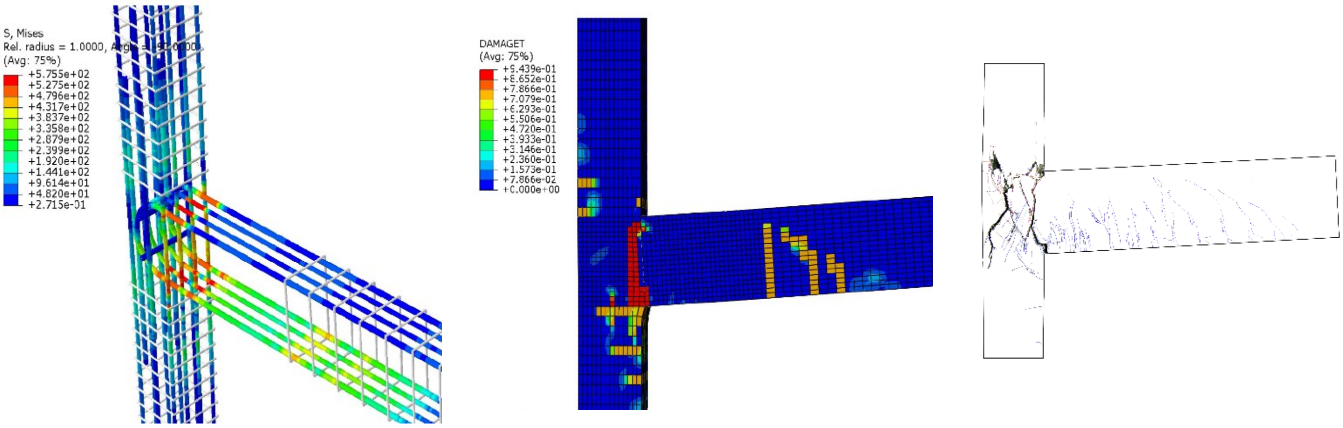

P = 178.73 kN P = 176.9 kN

d) Drift 6.5%

Fig. 10. (continued)

Table 3. Simulation results and experimental results of sample S3

Load direction		FEM/ Test			Secant hardness		
		25 mm	50 mm	100 mm	25 mm	50 mm	100 mm
Push direction	Average	0.97	1.09	1.19	0.97	1.09	1.10
	Difference (%)	-3.00	8.36	15.71	-2.74	8.59	16.02
Pull direction	Average	1.01	1.12	1.16	1.01	1.12	1.17
	Difference (%)	0.53	10.56	14.12	0.78	10.79	14.43

3.2. Parametric study

This section has demonstrated the reliability of the FE method using ABAQUS for simulating exterior beam-column joints. This section surveys the influence of three main parameters—UHPSFRC strengthening length, axial column load, and steel fiber content—on the principal tensile stress (pt) at the joint region. These parameters are crucial for assessing the shear resistance of joints designed for high ductility (DCH). Fig. 11 illustrates the schematic for this parametric study, guiding the analysis of each factor's impact.

3.2.1. Effect of UHPSFRC strengthening length

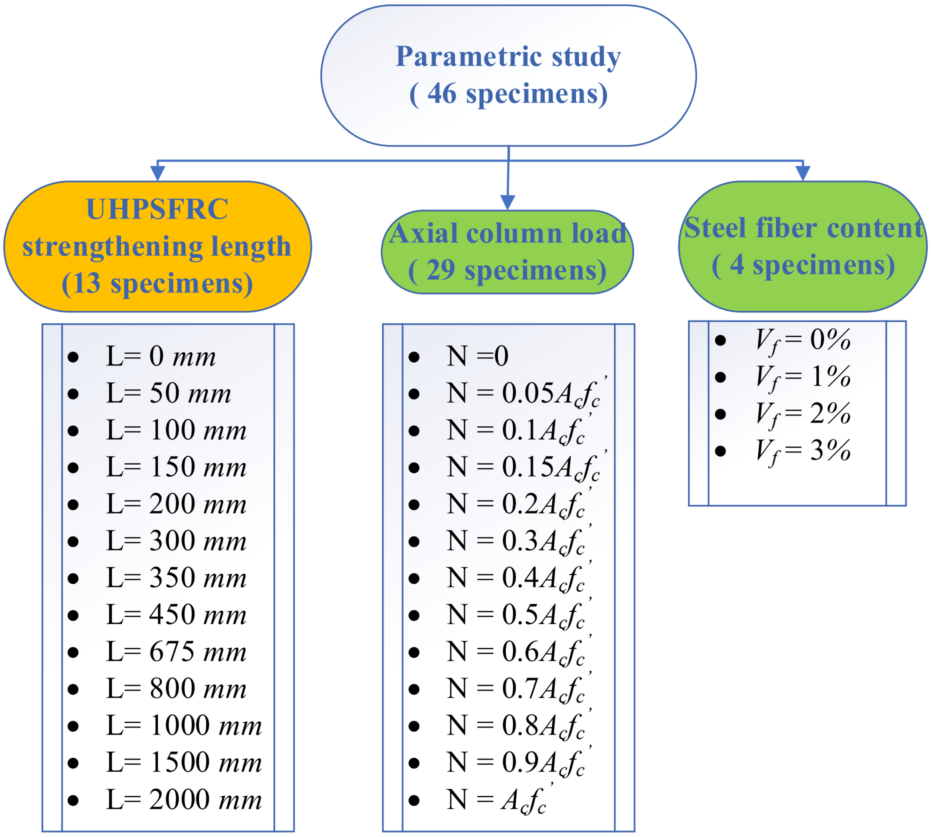

Fig. 11. Parameter survey diagram

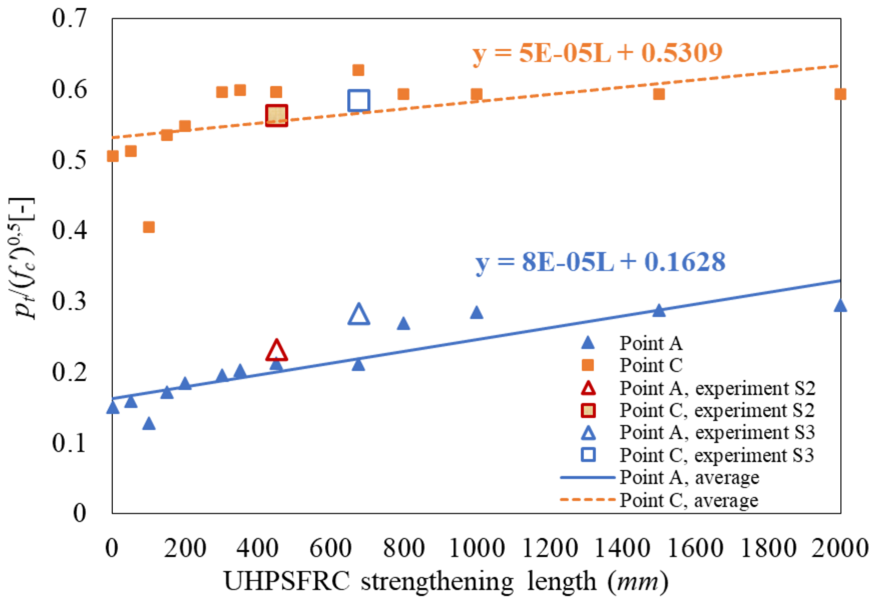

Fig. 12. Effect of UHPFRC length on the normalized principal tensile stress of the joint

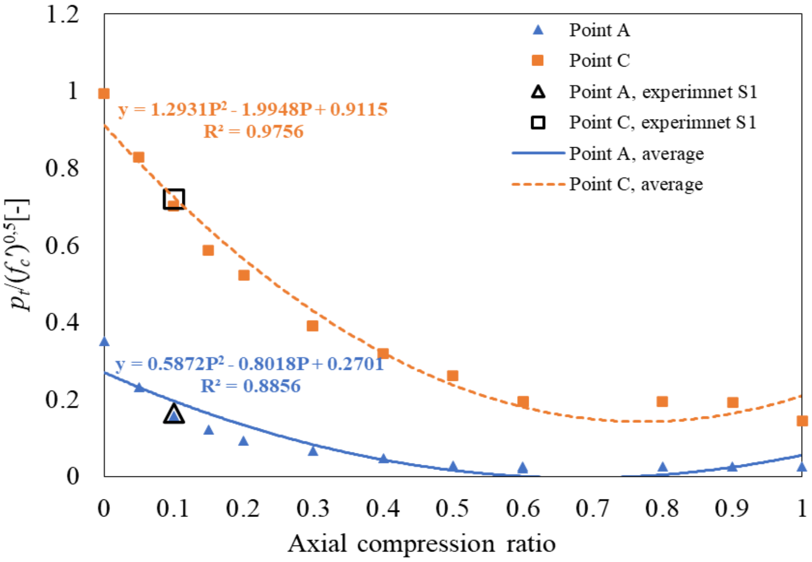

a) S1

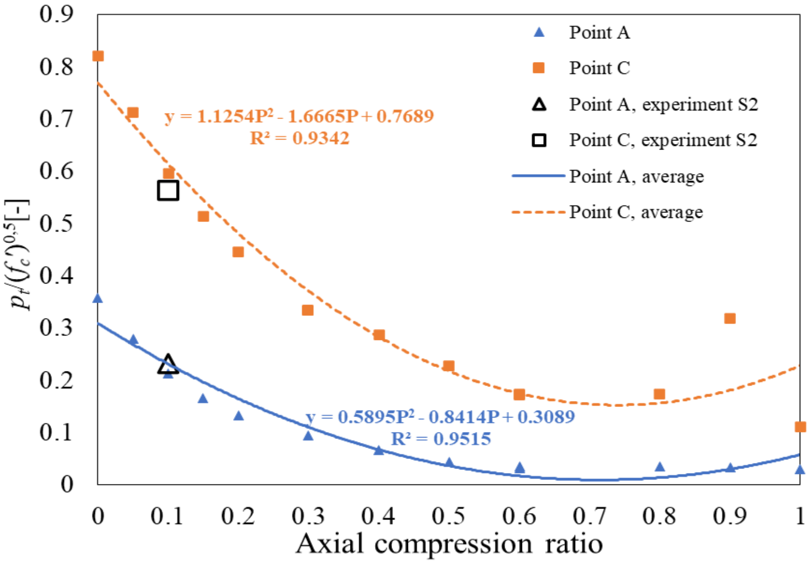

b) S2

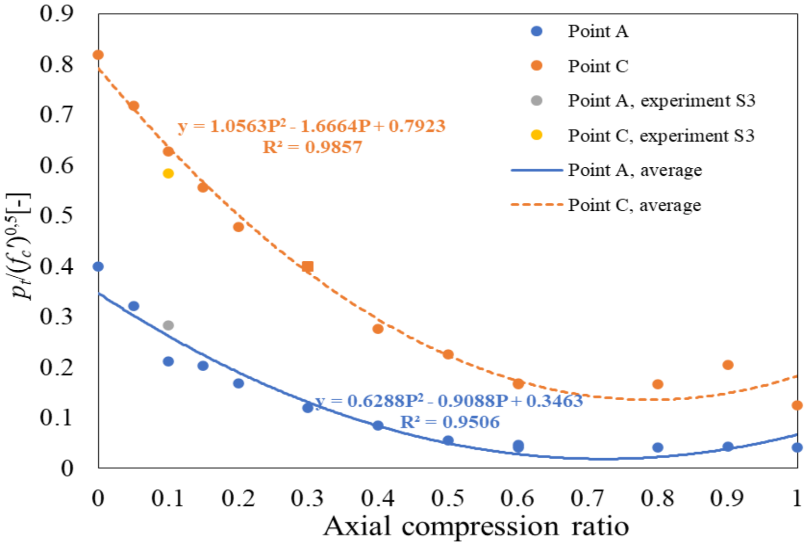

c) S3

Fig. 13. Effect of axial column load on the normalized principal tensile stress of the joint

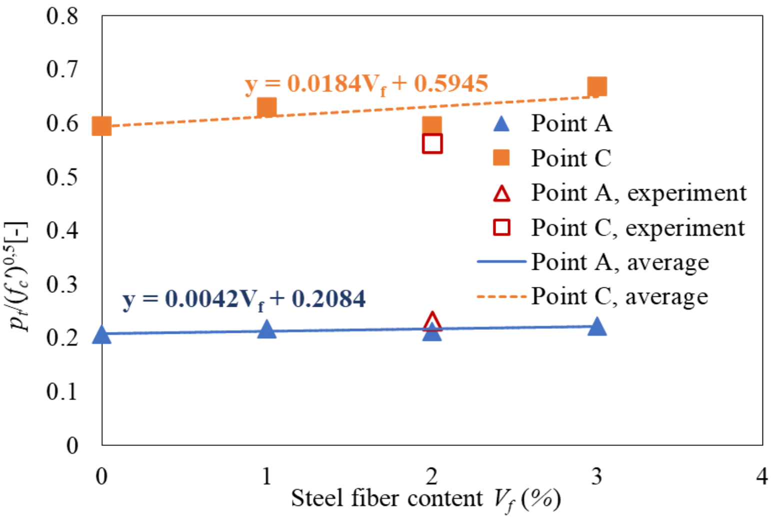

Fig. 14. Effect of steel fiber content on the normalized principal tensile stress of the joint

Table 4. UHPFRC concrete properties

Mixed name	Silica Fume (%)	Water/ adhesive	V_f (%)	f_c' (MPa)	E_c (MPa)
MRF0	25%	0.171	0	135.93	46262
MRF1	25%	0.175	1	144.57	47363
MRF2	25%	0.180	2	149.39	48295
MRF3	25%	0.187	3	151.62	48538

The variation in UHPSFRC strengthening length (L) was analyzed by adjusting the reinforced region from 0 to 2000 mm, covering the entire beam length. Fig. 12 presents the relationship between L and normalized principal tensile stress (p_t/f_c'). At the first crack (Point A), experimental results showed values of 0.35 for S2 and 0.38 for S3, while FE analysis yielded 0.36 and 0.39, respectively. At peak stress (Point C), experimental values were 0.65 for S2 and 0.68 for S3, with FE results at 0.66 and 0.70. The trends followed approximate equations: 5E-0.5L + 0.5309 for Point A and 8E-0.5L + 0.1628 for Point C. These results indicate that increasing the UHPSFRC length enhances both the initial tensile resistance and the maximum shear capacity of the joint, with a clear progression as the strengthened region extends, aligning closely with observed experimental behavior across the tested specimens.

3.2.2. Effect of axial column load

The influence of axial column load was explored by varying the load (N) from 0 to $A_g f_c'$, the column's full compressive capacity. Figs. 13a–c displays the relationship between the axial load ratio and normalized $\left(p_t / \sqrt{f'_c}\right)$ for S1, S2, and S3. For S1 at N = 650 kN, $\left(p_t / \sqrt{f'_c}\right)$ at Point A was 0.16 experimentally and 0.157 in FE, with a peak (Point C) of 0.75 experimentally and 0.70 in FE, following equations $0.5872P^2 - 0.8018P + 0.2701$ and $1.2931P^2 - 1.9948P + 0.9115$, respectively. For S2, Point A was 0.23 (experimental) and 0.21 (FE), and Point C was 0.56 (experimental) and 0.59 (FE), per $0.5895P^2 - 0.8414P + 0.3089$ and $1.1254P^2 - 1.16665P + 0.7689$. For S3, Point A was 0.28 (experimental) and 0.21 (FE), and Point C was 0.58 (experimental) and 0.62 (FE), per $0.6288P^2 - 0.9088P + 0.3463$ and $1.0563P^2 - 1.6664P + 0.7923$. At N = 975 kN (0.15 Agfc'), p_t at Point C increased by about 35% compared to S1, showing that axial load significantly affects shear strength, with nonlinear trends evident across all specimens.

3.2.3. Effect of steel fiber content

The steel fiber content (V_f) was varied from 0% to 3%, based on mix designs in Table 4, with results shown in Fig. 14. When studying the effect of this parameter, the steel fiber content in the UHPSFRC mix was chosen as presented in Table 4. At Point A (first crack), p_t/f_c' remained nearly constant at around 0.21 across all V_f levels, with k_a values of 0.216, 0.212, and 0.222 for 1%, 2%, and 3%, respectively, suggesting minimal influence on initial cracking. At Point C (peak stress), p_t increased linearly per $k_c = 0.0184 V_f + 0.5945$. For $V_f = 2\%$, p_t/f_c' was approximately 0.70, rising to 0.77 at $V_f = 3\%$, a 10% increase. The steel fiber content also affects the compressive strength of concrete, a parameter influencing shear stress at the point when the beam reinforcement stress reaches the yield limit (Point B) and at the peak shear stress (Point C). Kim and LaFave [9] demonstrated that joint shear stress is proportional to the square root of concrete compressive strength at Points B and C. In this study, joint strength, represented by the maximum normalized principal tensile stress (Point C), varies with steel fiber content. This indicates that higher fiber content modestly enhances peak tensile stress and shear capacity, primarily through improved post-crack behavior, though its effect is less pronounced compared to strengthening length and axial load. The FE model consistently captured these subtle changes, reflecting the experimental outcomes for varying fiber contents.

The parametric study reveals distinct influences of UHPSFRC strengthening length, axial column load, and steel fiber content on joint behavior. Extending the UHPSFRC length consistently increased p_t at both Points A and C, with a linear trend suggesting that longer reinforcement enhances joint stiffness and delays cracking. This aligns with the observed shift of plastic hinges to the beam in S2 and S3, indicating improved energy dissipation capacity. In contrast, axial column load exhibited a nonlinear effect, reducing p_t at Point A with increasing load due to early compressive stress dominance, yet significantly boosting peak p_t (up to 35% at $0.15f_c'A_g$) through confinement effects. This dual behavior underscores the need to optimize axial load levels to balance initial resistance and ultimate capacity. Steel fiber content had a limited impact on initial cracking but provided a modest linear increase in peak p_t, attributed to enhanced concrete compressive strength and fiber bridging. The varying magnitudes of influence—length being most significant, followed by axial load, and then fiber content—suggest that strengthening strategies should prioritize UHPSFRC application extent, with load and fiber adjustments as supplementary enhancements.

4. Concluding remarks

This study underscores the potential of UHPSFRC in improving the seismic resilience of exterior beam-column joints through FE analysis in ABAQUS. The validated model effectively simulated joint behavior, confirming UHPSFRC's role in enhancing ductility and shear resistance under cyclic loading. Fracture energy and drift capacity were accounted for in calibrating the CDP model, supporting improved resilience. Parametric findings highlight the critical influence of strengthening length, axial load, and fiber content on principal tensile stress, offering a framework for optimizing retrofit designs. These insights contribute to advancing seismic engineering practices, particularly in regions prone to earthquakes, by demonstrating a cost-effective alternative to extensive experimental testing. The FE approach's accuracy in capturing complex stress-strain interactions positions it as a valuable tool for future research. Further investigations could explore additional factors, such as reinforcement anchorage or joint geometry variations, to refine UHPSFRC applications. Expanding the parametric scope to include long-term durability and multi-hazard scenarios could also broaden the practical applicability of these findings, supporting the development of robust, resilient RC structures.

References

[1]. X. Su, H. Yang, Q. Liu, X. Wang, J. Fu. (2024). Experimental study on seismic behavior of reinforced concrete exterior beam-column

joints under varying axial load. *Engineering Structures*, 318, 118682.
[2]. B.-T. Zheng, B. Gencturk, H. Aryan, X. Pan, J. Lopez, J. Rivera, M.D. Carpio, T. Alkhrdaji. (2024). Seismic Performance of Highly Eccentric Reinforced Concrete Beam–Column Joints. *Journal of Structural Engineering*, 150(11), 04024161.
[3]. Z.F. Akbulut, T.A. Tawfik, P. Smarzewski, S. Guler (2025). Advancing Hybrid Fiber-Reinforced Concrete: Performance, Crack Resistance Mechanism, and Future Innovations. *Buildings*, 15(8), 1247.
[4]. T. Paulay, R. Park, M.J.N. Preistley. (1978). Reinforced concrete beam-column joints under seismic actions. *Journal Proceedings*, 75(11), 585-593.
[5]. S. Hakuto, R. Park, H. Tanaka. (2000). Seismic load tests on interior and exterior beam-column joints with substandard reinforcing details. *Structural Journal*, 97(1), 11-25.
[6]. X. Qin, S. Kaewunruen (2024). Machine learning and traditional approaches in shear reliability of steel fiber reinforced concrete beams. *Reliability Engineering & System Safety*, 251, 110339.
[7]. P. Chetchotisak, J. Teerawong, C. Hansapinyo. (2024). Strut-and-tie model including shear–flexure interaction for predicting shear capacity of reinforced concrete short coupling beams. *Structures*, 66, 106791.
[8]. R. Valente, M. Pimentel. (2024). Fibre reinforced concrete under in-plane shear stresses. *Engineering Structures*, 307, 117890.
[9]. F. Kazemi, T. Shafighfard, D.-Y. Yoo. (2024). Data-Driven Modeling of Mechanical Properties of Fiber-Reinforced Concrete: A Critical Review. *Archives of Computational Methods in Engineering*, 31, 2049–2078.
[10]. B. Borah, H.B. Kaushik, V. Singhal. (2023). Analysis and Design of Confined Masonry Structures: Review and Future Research Directions. *Buildings*, 13(5), 1282.
[11]. A. Deifalla. (2021). A mechanical model for concrete slabs subjected to combined punching shear and in-plane tensile forces. *Engineering Structures*, 231, 111787.
[12]. S. Barbhuiya, B.B. Das, F. Kanavaris. (2024). A review of fracture propagation in concrete: fundamentals, experimental techniques, modelling and applications. *Magazine of Concrete Research*, 76(10), 482-514.
[13]. L. Duan, Y. Zhang, L. Yan, S. Bao, H. Liu, J. Lu. (2025). Investigation on the crack development behaviour of CFRP strengthened RC beams under static and impact loading. *Engineering Failure Analysis*, 171, 109369.
[14]. ACI. (2014). Building code requirements for structural concrete. *American Concrete Institute*.
[15]. NZS. (1995). Concrete structures standard. *Standards New Zealand*.
[16]. A. Masi, G. Santarsiero, D. Nigro. (2013). Cyclic Tests on External RC Beam-Column Joints: Role of Seismic Design Level and Axial Load Value on the Ultimate Capacity. *Journal of Earthquake Engineering*, 17(1), 110-136.
[17]. J. Yang, J. Xia, Z. Zhang, Y. Zou, Z. Wang, J. Zhou. (2022). Experimental and numerical investigations on the mechanical behavior of reinforced concrete arches strengthened with UHPC subjected to asymmetric load. *Structures*, 39, 1158-1175.
[18]. S. Kim, J. Shin, W. Kim. (2024). Assessing the Seismic Performance of Exterior Precast Concrete Joints with Ultra-High-Performance Fiber-Reinforced Concrete. *International Journal of Concrete Structures and Materials*, 18, 10.
[19]. L. Chen, J. Xu, H. Wu. (2023). Cyclic behavior of UHPSFRC-strengthened RC joints: Influence of fiber content and joint detailing. *Construction and Building Materials*, 405, 133245.
[20]. H. Jiang, C. Huang, G. Mei, X. Gao, Y. Tian, X. Sun. (2023). Experimental and numerical investigations on direct shear performance of

UHPC dry joints. *Engineering Structures*, 283, 115872.

[21]. H. Abdelbaset, B. Cheng, S. Xiang, L. Tian. (2023). An investigation on fatigue crack propagation behavior of welded connections in UHPC reinforced OSDs using 3D crack simulation. *Structures*, 50, 1527-1544.